Since January 2020 Elsevier has created a COVID-19 resource centre with free information in English and Mandarin on the novel coronavirus COVID-19. The COVID-19 resource centre is hosted on Elsevier Connect, the company's public news and information website.

International Journal of Pharmaceutics 624 (2022) 121971

Contents lists available at ScienceDirect

International Journal of Pharmaceutics

journal homepage: www.elsevier.com/locate/ijpharm

Neutrophil membrane-coated therapeutic liposomes for targeted treatment in acute lung injury

Zhiwei Huang [a,b,c], Hengcai Wang [c], Juan Long [a,d], Zhongqiu Lu [a,d], Changju Chun [b,*], Xinze Li [a,d,*]

[a] Department of Emergency, the First Affiliated Hospital of Wenzhou Medical University, Wenzhou 325035, China
[b] Research Institute of Pharmaceutical Sciences, College of Pharmacy, Chonnam National University, Gwangju 61186, Republic of Korea
[c] School of Pharmaceutical Sciences, Wenzhou Medical University, Wenzhou 325035, China
[d] Wenzhou Key Laboratory of Emergency and Disaster Medicine, Wenzhou 325035, China

ARTICLE INFO

Keywords:
Neutrophil membrane
Biomimetic drug carriers
Acidic fibroblast growth factor
Pulmonary inflammation

ABSTRACT

Acute lung injury (ALI) is one of the most common comorbidities associated with sepsis and can lead to acute respiratory distress syndrome. Intense inflammatory response due to excessive activation and uncontrolled infiltration of neutrophils are the central processes in the development of sepsis-induced ALI. In this study, a biomimetic nanoplatform that is a neutrophil membrane-coated liposome-loaded acidic fibroblast growth factor (aFGF@NMLs), which can selectively target the inflamed lung and effectively alleviate sepsis-induced ALI via inflammation suppression, was constructed. *In vitro* findings revealed that aFGF@NMLs has pro-inflammatory cytokine binding capabilities and can promote cellular uptake, substantially attenuate inflammatory responses, and enhance cellular antioxidant capacity. The *in vivo* results show that aFGF@NMLs can specifically accumulate in injured lungs in ALI mice after intravenous injection, thereby reducing the secretion of pro-inflammatory cytokines, inhibiting pulmonary cell apoptosis, and promoting lung function recovery. In conclusion, aFGF@NMLs demonstrated anti-inflammatory effects, mitigated the progression of ALI, and contributed to the disease prognosis. This research offers an innovative strategy and concept for the clinical treatment of diseases related to pulmonary inflammation.

1. Introduction

In sepsis, the lung is the most susceptible target organ and undergoes sepsis-induced acute lung injury (ALI) as described by Wu et al. (2007). Sepsis-induced ALI is characterized by malfunction of both pulmonary and immune cells, resulting in reduced lung compliance, hypoxemia, and pulmonary edema (Xiong et al., 2020). During sepsis, inflammatory cells generate excessive pro-inflammatory molecules that stimulate the recruitment and activation of neutrophils and macrophages in the lung (Sun et al., 2018; Wang et al., 2019). These cells then produce cytokines, chemokines, oxygen radicals, and proteases, all of which lead to amplification of inflammatory responses and cause damage to both alveolar epithelial and vascular endothelial cells in lung (Gong et al., 2017). As the permeability of the lung increases, significant volumes of fluid containing proteins and inflammatory cells enter the lung tissue at a rapid rate, causing osmotic pulmonary edema, hyaline membrane formation and alveolar collapse with development of interstitial lung fibrosis (Ren et al., 2021). Currently, the treatment of septic ALI focuses on ensuring adequate oxygen supply to tissues and cells, such as mechanical ventilation therapy with ventilator including high-flow nasal cannula and extracorporeal membrane oxygenation (Fan et al., 2018; Mauri et al., 2017). However, mechanical ventilation improves the oxygenation status of the patient while concurrently being detrimental to the organism. The mechanical tension created by excessive mechanical ventilation can lead to lung inflammation and is an important cause of lung injury (Keszler, 2017). Therefore, exploring alternative treatment methods from an anti-inflammatory perspective will be extremely important for bringing about a decrease in morbidity and mortality associated with sepsis-induced ALI (Chen et al., 2020b).

Since the first purification of acidic fibroblast growth factor (aFGF) from bovine brain in 1984, aFGF has been shown to promote injury repair and pro-angiogenesis (Chen et al., 2020a; Wu et al., 2011). As an

* Corresponding authors at: Department of Emergency, the First Affiliated Hospital of Wenzhou Medical University, Wenzhou 325035, China (X. Li). Research Institute of Pharmaceutical Sciences, College of Pharmacy, Chonnam National University, Gwangju 61186, Republic of Korea (C. Chun).
E-mail addresses: cchun1130@chonnam.ac.kr (C. Chun), lxzpharm@163.com (X. Li).

https://doi.org/10.1016/j.ijpharm.2022.121971
Received 27 April 2022; Received in revised form 22 June 2022; Accepted 29 June 2022
Available online 3 July 2022

autocrine/paracrine regulator, aFGF can promote cell proliferation and has been used clinically to promote wound repair and ulcer regeneration. Recent studies have discovered that aFGF possesses anti-inflammatory properties, for example, Liang et al. (2018) found that aFGF alleviated diabetic nephropathy by countering inflammatory signaling cascades in injured renal tissue via suppressing nuclear factor kappa B (NF-κB) and c-Jun N-terminal kinase signaling pathways. The previous studies indicate that aFGF could ameliorate diabetic endothelial dysfunction by suppressing mitochondrial oxidative stress and aFGF could effectively prevent retinal injury in diabetes by reducing the cascade of oxidative stress and inflammatory signals in neuroretina tissue (Huang et al., 2021a; Sun et al., 2021). Activation of FGF signaling after aFGF injection also inhibited acute pancreatitis-induced inflammation response and effectively protected pancreatic tissue (Tu et al., 2020). This evidence shows that aFGF has promising applications in the treatment of inflammatory diseases. However, as a peptide, aFGF has low stability, short biological half-life, and is rapidly degraded *in vivo*, all of which limit its clinical applications (Wang et al., 2017). Additionally, the limited distribution and low concentration of aFGF in the focal area after administration contribute to the lack of satisfactory therapeutic effects by aFGF. Therefore, it is urgent to develop a safe and efficient drug carrier for effectively delivery of aFGF *in vivo* to treat inflammation-related diseases, such as sepsis-induced ALI.

The main pathological feature of ALI is the excessive accumulation and activation of neutrophils in the lung tissue (Grommes and Soehnlein, 2011). Neutrophils exert pro-inflammatory effects in the ALI by releasing proteases, cytokines, and reactive oxygen species (ROS), all of which further aggravate tissue damage. In the presence of ALI, activated macrophages release tumor necrosis factor alpha and interleukin 1 beta (TNF-α and IL-1β, respectively) leading to the increased production of chemokines by capillary endothelial cells and alveolar epithelial cells in the lung, activation of the inflammatory response, and promotion of continuous recruitment of neutrophils to the inflamed lung (Park et al., 2019; Zemans et al., 2009). It may be possible to design lung-targeted drug delivery systems by taking advantage of the fact that large aggregation of neutrophils can be found in an injured lung.

In recent years, researchers have utilized neutrophil membrane (NM) to construct drug carriers and develop biomimetic drug delivery system with neutrophil characteristics (Jin et al., 2018; Kang et al., 2017; Xie et al., 2022). Neutrophils bind to inflamed cells via adhesion molecules, such as intercellular adhesion molecule-1 (ICAM-1), and then move to inflammatory sites (Zhao et al., 2019). Previous studies have shown that synthetic nanoparticles decorated with neutrophil membranes can target inflamed brain microvascular endothelial cells after a stroke (Feng et al., 2021). In addition, the NM-coated nanoparticles were found to show significant therapeutic efficacy in rheumatoid arthritis and acute pancreatitis due to their inflammation-targeted capability (Zhang et al., 2018; Zhou et al., 2019a). Incorporation of NM into liposomes or nanoparticles that inherit the neutrophil's antigenic exterior and related membrane functions can be used to create neutrophil-targeted biological carriers, which are similar to neutrophils, and can specifically accumulate in inflamed diseased sites,

In this study, a neutrophil membrane-coated liposome loaded aFGF (aFGF@NMLs) used as a biomimetic nanoplatform for treating sepsis-induced ALI (Scheme 1) is reported. In this study, aFGF liposomes (aFGF@Lips) were prepared after which the extracted NM was inlaid in aFGF@Lips to construct the aFGF@NMLs. It was found that aFGF@NMLs could specifically target inflamed lung that contained abundant neutrophils for effective delivery of aFGF. *In vitro* experimental results demonstrated the cytoprotective effects of aFGF@NMLs that could effectively inhibit inflammatory responses and improve cellular antioxidant capacity. After intravenous administration, aFGF@NMLs selectively accumulated in injured lungs of the ALI model and improved the therapeutic effect of aFGF on ALI. It is believed that this strategy will provide an applicative perspective for lung-targeted therapy.

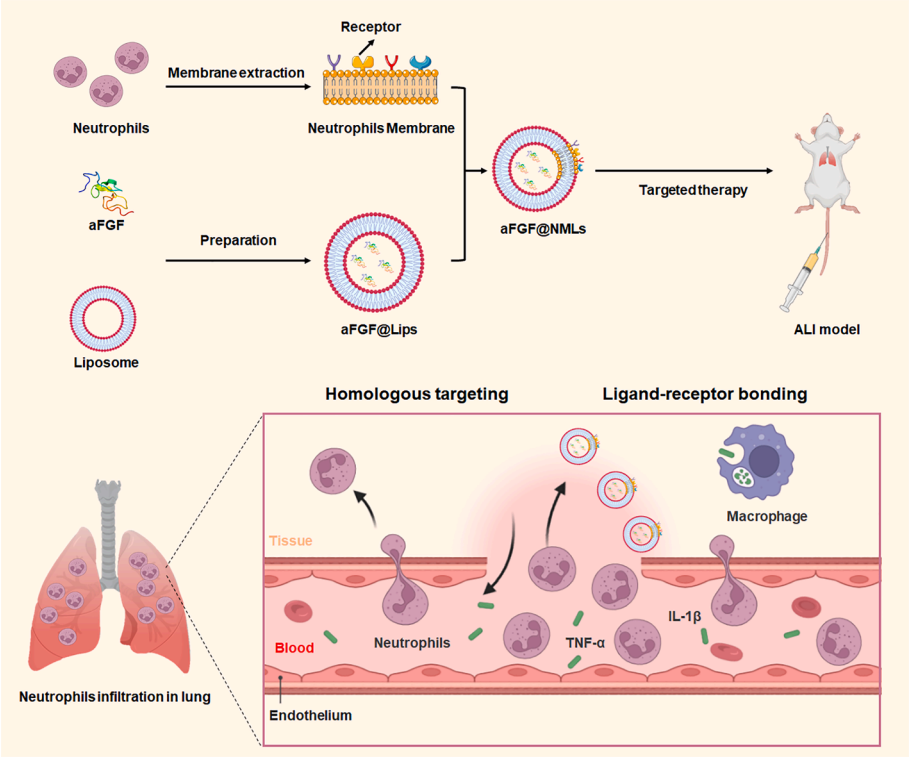

Scheme 1. Targeted therapy of neutrophil membrane-coated liposome loaded acidic fibroblast growth factor (aFGF@NMLs) for treating sepsis-induced acute lung injury (ALI).

2. Materials and methods

2.1. Materials, cells, and animals

aFGF was provided by Wenzhou Medical University (Wenzhou, China). Malondialdehyde (MDA) assay kit, hematoxylin and eosin (H&E) staining kit, fluorescein isothiocyanate (FITC), superoxide dismutase (SOD) activity kit, terminal deoxynucleotidyl transferase dUTP nick end labeling (TUNEL) apoptosis assay kit, high mobility group box-1 (HMGB-1) enzyme-linked immunosorbent assay (ELISA) kits, lipopolysaccharides (LPS) and 4′,6-diamidino-2-phenylindole (DAPI) solution were purchased from Solarbio Science & Technology Co., Ltd (Beijing, China). Egg yolk lecithin and cholesterol were obtained from Shanghai Advanced Vehicle Technology Pharmaceutical Co., Ltd (Shanghai, China). Bicinchoninic acid (BCA) protein assay kit, ROS assay kit and cell membrane fluorescent probe (DiI) were obtained from Beyotime Biotechnology Co., Ltd (Shanghai, China). Cell culture plates, coverslips, and centrifuge tubes were obtained from NEST Biotechnology Co., Ltd. (Wuxi, China). Cell counting kit-8 (CCK-8) was purchased from Yeasen Biotechnology Co., Ltd. (Shanghai, China). IL-1β, IL-6 and TNF-α ELISA kits were obtained from Multisciences Biotechnology Co., Ltd. (Hangzhou, China). Lymphocyte function-associated antigen-1 (LFA-1) antibody was purchased from BioLegend (San Diego, USA). IL-1 receptor (IL-1R) antibody was purchased from R&D Systems (Minneapolis, USA). TNF-α receptor (TNF-αR), CD68, CD11β, IL-6, TNF-α, glyceraldehyde 3-phosphate dehydrogenase (GAPDH), and HMGB-1 antibody were obtained from Abcam (MA, USA). Ly6G antibody was obtained from Santa Cruz Biotechnology (TX, USA). The endotoxin quantitation kit was purchased from Thermo Scientific (Shanghai, China).

The human bronchial epithelial cell line (BEAS-2B) was obtained from Cell Bank of the Chinese Academy of Sciences (Shanghai, China). The cells were cultured in DMEM supplemented with 10% (v/v) FBS, 100 U/mL penicillin, and 100 μg/mL streptomycin in an incubator with 5% CO_2 at 37 °C.

Male C57BL/6N mice (20–30 g) were provided by Shanghai Laboratory Animal Center (Shanghai, China). All animal protocols were conducted with the consent of the Animal Care and Use Committee of Wenzhou Medical University and were complied with the National Research Council's Guide for the Care and Use of Laboratory Animals.

2.2. Extraction of the neutrophil membrane

Neutrophils were obtained according to previously described methods (Zhao et al., 2019). The neutrophils were stimulated with lipopolysaccharide ([LPS] 1 μg/mL) for 4 h at 37 °C after which cells were washed six times with phosphate-buffered saline (PBS) for 5 min each to ensure removal of LPS. After that, the neutrophil membrane (NM) was isolated from the stimulated cells. Briefly, neutrophils were treated with the hypotonic lysing buffer and then underwent ultrasonication to promote cell lysis. Subsequently, the suspension was centrifuged (1500 *g*, 5 min) at 4 °C to remove unbroken nuclei and cells. The resulting supernatant was centrifuged again (12,000 *g*, 30 min) to obtain high-purity NM. According to the instructions, the LPS content in the extracted NM was also detected by an endotoxin quantitation kit.

2.3. Preparation of aFGF@NMLs

Firstly, aFGF-loaded liposomes (aFGF@Lips) were prepared using the reverse-phase evaporation method (Zhao et al., 2019). Briefly, 9 mg egg phosphatidylcholine and 1 mg cholesterol were completely solubilized in 5 mL dichloromethane after which aFGF solution (1 mg/mL) was added to the mixture while undergoing ultrasonication (50 W, 2 min). After that, a rotary evaporator was used to remove the organic solvent from the solution. Subsequently, the sample was rehydrated with PBS and homogenized while undergoing ultrasonication (50 W, 10 min) to obtain aFGF@Lips. Eventually, the NM coating the aFGF@Lips extruded from the polycarbonate membrane (100 nm) and was used to prepare aFGF@NMLs. The ratio of NM to lipid was 1:50 that was used to prepare the aFGF@NMLs following previous research methods (Zhao et al., 2019). The blank liposomes (Lips) and blank neutrophil membrane-coated liposomes (NMLs) without aFGF were also prepared by the same procedure.

2.4. Characterization of aFGF@NMLs

A series of aFGF@NMLs was prepared, and the encapsulation efficiency (EE%) and loading capacity (LC%) of these aFGF@NMLs were evaluated to obtain the appropriate proportion of aFGF@NMLs. The samples were centrifuged at 12,000 g for 20 min, and the content of aFGF in the supernatant was measured by the ELISA kit. EE% = (total aFGF amount − free aFGF amount in supernatant)/total aFGF amount) × 100%. LC% = (total aFGF amount − free aFGF in supernatant)/total aFGF@NMLs amount).

The dynamic light scattering detector was used to measure the size distribution, polydispersity index (PDI), and zeta potentials of aFGF@Lips and aFGF@NMLs. The morphologies of aFGF@Lips and aFGF@NMLs were observed using a transmission electron microscope (TEM).

The release profile of aFGF *in vitro* was evaluated by the dynamic dialysis method. Briefly, aFGF, aFGF@Lips, and aFGF@NMLs were transferred into a dialysis bag (100 kDa) and dialyzed in PBS. The set was put on a magnetic stirrer with rotating speed of 100 rpm. The release medium was collected to determine the concentration of aFGF at each specified time point.

The aFGF@NMLs was dispersed in PBS containing different concentrations of fetal bovine serum (FBS), and the change of particle size and PDI of samples were then recorded for seven days to assess the stability of aFGF@NMLs.

Western blotting was used to detect the typical markers of neutrophil on NM and aFGF@NMLs followed the method previously described (Liu et al., 2020). For the pro-inflammatory cytokine binding assay, the recombinant mouse IL-1β or TNF-α (20 ng/mL) was mixed with the aFGF@Lips or aFGF@NMLs. The samples were placed in a thermostat (37 °C) for 90 min and then centrifuged at 12,000 *g* for 5 min. The supernatant was collected, and the remaining proteins were determined by corresponding ELISA kits.

2.5. Cell proliferation activity and hemocompatibility of aFGF@NMLs

The BEAS-2B cells were seeded in 96-well and cultured for 24 h. Then cells were treated with different concentrations (5–200 ng/mL) of blank Lips blank NMLs, aFGF, aFGF@Lips, or aFGF@NMLs for 24 h after which the cell viability of each group was evaluated.

For the hemocompatibility test, erythrocyte solutions (2%) containing deionized water (positive control), 0.9% NaCl (negative control), aFGF, aFGF@Lips, or aFGF@NMLs (200 ng/mL) were incubated at 37 °C for 2 h. Subsequently, these samples were centrifuged at 1000 g for 5 min, the collected supernatants were measured using an ultraviolet spectrophotometer (Varian, Palo Alto, CA, USA) at 576 nm to obtain the absorbance values of each group, and the hemolysis rates were calculated by mean absorbance measured from each group according to the equation: hemolysis rate (%) = $(OD_{samples} - OD_{negative\ control})/(OD_{positive\ control} - OD_{negative\ control}) \times 100\%$.

2.6. Fluorescent observation of aFGF@NMLs

According to previous study, the aFGF that was labeled by FITC, and NM was labeled by DiI (Zhao et al., 2019), then prepare the fluorescence-labeled aFGF@NMLs. The RAW 264.7 cells were then incubated with fluorescent aFGF@NMLs for 10 min and observed using a fluorescent microscope (Olympus Corp., Tokyo, Japan).

2.7. Cellular uptake aFGF@NMLs

The FITC-labeled aFGF was obtained using the standard method according to previous study (Xu et al., 2018; Zhao et al., 2019) after which the fluorescence-labeled aFGF was used to prepare aFGF@Lips and aFGF@NMLs. The BEAS-2B cells were first stimulated by LPS (10 μg/mL) for 12 h to activate the inflammatory microenvironment. LPS-stimulated cells were treated with FITC-labeled aFGF, aFGF@Lips, or aFGF@NMLs (100 ng/mL) for 1, 2, and 4 h. After washing with PBS, the cells were treated with DAPI to reveal the nucleus and then observed by a confocal laser scanning microscope (Olympus Corp., Tokyo, Japan). In addition, flow cytometry was also performed to evaluate intracellular fluorescence. As a comparison, the cells not treated with LPS were also incubated with FITC-labeled aFGF, aFGF@Lips, or aFGF@NMLs (100 ng/mL) for 4 h, and the intracellular fluorescence was observed.

2.8. Cytoprotective capacity of aFGF@NMLs

The BEAS-2B cells were treated with aFGF, aFGF@Lips, or aFGF@NMLs (100 ng/mL) in the presence of LPS (10 μg/mL) for 24 h. After incubation, ROS production in cells was detected by the fluorescent probe DCFH-DA and observed by a fluorescent microscope (Olympus Corp., Tokyo, Japan). Images from each group were recorded, and the fluorescent intensity was quantified. The cell viability of each group was measured, and the contents of SOD and MDA in cells were measured by the corresponding reagent kits. In addition, the culture supernatants were also collected, and the levels of HMGB-1, IL-1β, IL-6, and TNF-α were measured using ELISA kits.

2.9. Animal model

A cecal ligation and puncture (CLP)-induced sepsis murine model was used in this study, and a disease model was established was according to the previous methods (Rittirsch et al., 2009). Mice were anesthetized, the skin surface of the abdomen was disinfected, and skin was cut open. Part of the cecum was brought out of the peritoneal cavity and ligated it with a 6–0 silk thread, and a single puncture with a dual hole in distal cecum was made using 21-gauge needles. After puncture, the cecum was gently squeezed to extrude any feces. After that step, the cecum was returned to the peritoneal cavity, and the abdominal musculature and skin were closed. Subsequently, mice were injected with 0.3 saline subcutaneously for fluid resuscitation. The mice in the control group, except for the CLP group, also underwent the same surgical procedure.

The sepsis-induced ALI models were divided into five groups with three mice per group: (1) Control group + saline; (2). ALI + saline; (3). ALI + aFGF (1 mg/kg, intravenous [iv]); (4). ALI + aFGF@Lips (dose equivalent to aFGF 1 mg/kg, iv); and (5). ALI + aFGF@NMLs (dose equivalent to aFGF 1 mg/kg, iv). The treatment group was injected with aFGF, aFGF@Lips, or aFGF@NMLs 30 min before and 3 h after the CLP procedure according to previous studies with proper adjustments (Zheng et al., 2020). All mice were sacrificed 24 h after CLP, and the lung tissue, other organ, blood samples, and bronchoalveolar lavage fluid (BALF) was obtained for further measurements. The levels of liver and kidney function indices in blood of each group were analyzed at the First Affiliated Hospital of Wenzhou Medical University.

2.10. Distribution of aFGF@NMLs

The ALI mice were intravenously injected with FITC-labeled aFGF, aFGF@Lips, or aFGF@NMLs, and after 2, 4, and 8 h, the mice were sacrificed, and the major organs were removed to observe fluorescent signals using an imaging system (PerkinElmer, MA, USA). Blood samples were also collected to measure the concentration of aFGF in blood using the appropriate ELISA kit.

2.11. Assessment of lung tissue

H&E staining and TUNEL assay were used for the histological analysis. The scoring system of lung tissue was based on cell infiltration and hyperplasia, alveolar hemorrhage, and alveolar septal thickening (Wu et al., 2019). The levels of cells and protein in the BALF were measured by flow cytometry and BCA protein assay kit. The dry and wet weights of lung tissue were recorded, and the ratio of wet weight to dry weight (W/D) was calculated to assess pulmonary edema. An Evans blue extravasation assay was conducted to determine the pulmonary vascular permeability of each group as the previous method (Jin et al., 2020). The mice were injected with Evans blue (20 mg/kg) and sacrificed after 30 min after which the lung tissue was removed for Evans blue measurement. Immunohistochemistry was performed to detect the levels of CD68, IL-6, TNF-α, and HMGB-1 in the lung tissue. The production of CD68 and TNF-α in kidneys and livers were also determined by immunohistochemistry and ELISA kits.

2.12. Statistical analysis

Data are presented as the mean value ± standard deviation (SD). Statistical analysis was performed using student's *t*-test and one-way analysis of variance (ANOVA). Values of $^{*}P \leq 0.05$ and $^{**}P \leq 0.01$ were considered statistically significant.

3. Results and discussion

3.1. Characterization of aFGF@NMLs

Before preparing aFGF@NMLs using NM, the LPS residue in the extracted NM and the NMLs were evaluated. The results of the LPS test showed that the content of LPS in the NM and the NMLs were below the lower limit of detection (<0.01 endotoxin units [EU]/mL), which meant that no residual LPS in the NM and the NMLs could be detected.

A series of aFGF@NMLs was prepared by adding 5, 7.5, 10, 12.5, and 15 μg of aFGF per 10 mg of NMLs. The encapsulation efficiency (EE%) and loading capacity (LC%) of these aFGF@NMLs were shown in Fig. S1. According to these data, 10 μg aFGF and 10 mg NMLs (the ratio of NM/lipid = 1:50) were used to prepare the aFGF@NMLs. The EE% and LC% of aFGF@NMLs prepared at this ratio were 94.3 ± 1.9% and 0.098 ± 0.004%, respectively.

The hydrodynamic radius of aFGF@Lips and aFGF@NMLs were 87.5 ± 1.6 nm and 107.4 ± 2.7 nm, respectively. As shown in Fig. 1A, the distribution curve of aFGF@NMLs shifted to the right, which indicated that its particle size increased due to wrapping of the NM. The PDI of aFGF@Lips and aFGF@NMLs were 0.125 ± 0.008 and 0.137 ± 0.014, respectively. The zeta potential of the extracted NM was −14.6 ± 1.5 mV, which did not significantly affect the zeta potential of aFGF@NMLs at this preparation ratio of NM and lipid (1:50). As shown in Fig. 1B, the zeta potential of aFGF@NMLs was −12.2 ± 1.9 mV, which was comparable to that of aFGF@Lips (−12.9 ± 2.1 mV). The micromorphological features of aFGF@Lips and aFGF@NMLs were visualized using TEM after uranyl acetate staining. The image of aFGF@Lips showed a typical spherical structure, whereas aFGF@NMLs exhibited a spherical core–shell structure, and the white arcs represented unilamellar NM coating around the liposome (Fig. 1C). The *in vitro* release behavior of aFGF@NMLs was also investigated. As depicted in Fig. 1D, aFGF was released rapidly, reaching a value greater than 80% within 12 h. In comparison, aFGF@Lips showed a distinct sustained release pattern, and the aFGF@NMLs was released more slowly under the obstruction of membrane, thereby avoiding the significant loss of aFGF due to the abrupt release and failure to achieve satisfactory therapeutic benefits (Zhao et al., 2016). In addition, the size and PDI of aFGF@NMLs in different concentrations of FBS were measured daily for seven days to assess the stability of aFGF@NMLs (Huang et al., 2021b). During the observation period, no discernible changes in the sizes and PDIs of

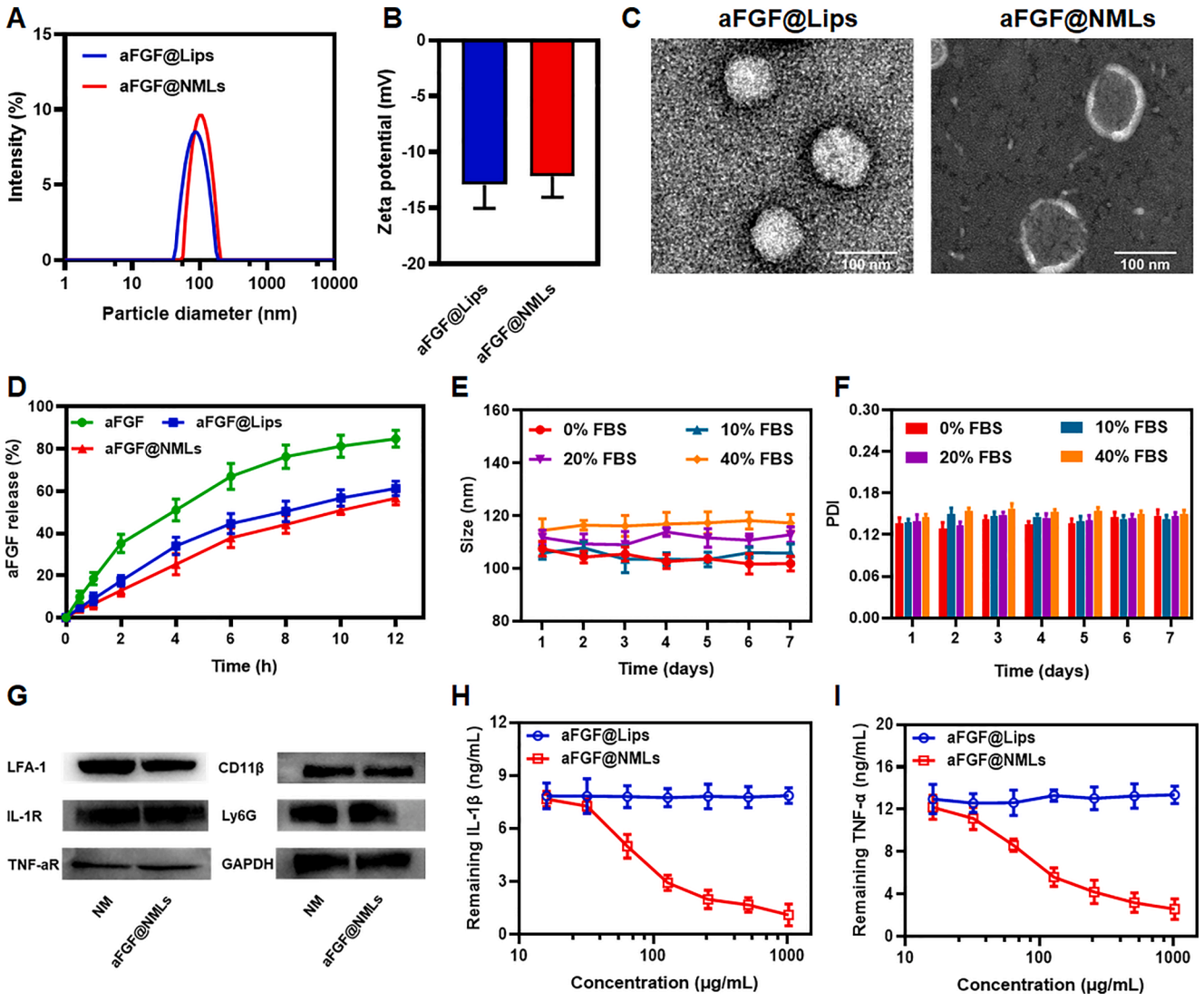

Fig. 1. Characterization of aFGF@NMLs. (A) The distribution of particle size and (B) zeta potential of aFGF@Lips and aFGF@NMLs. (C) Representative transmission electron microscopy (TEM) images of aFGF@Lips and aFGF@NMLs. (D) *In vitro* release profile of aFGF, aFGF@Lips, and aFGF@NMLs. The change in (E) size and (F) polydispersity index (PDI) of aFGF@NMLs in phosphate-buffered saline (PBS) containing various concentrations of fetal bovine serum (FBS) for seven days. (G) Characteristic protein bands of neutrophil membrane (NM) and aFGF@NMLs determined by western blotting. Binding capacity of aFGF@Lips and aFGF@NMLs with (H) interleukin 1 beta (IL-1β) and (I) tumor necrosis alpha (TNF-α). Data are expressed as the mean ± standard deviation (SD) for three samples.

aFGF@NMLs were detected, indicating that the aFGF@NMLs were stable (Fig. 1E,F). The results of immunoblotting showed the markers LFA-1, IL-1R, TNF-αR, CD11β, and Ly6G existed in the NM and aFGF@NMLs, verifying the translocation of NM into the aFGF@NMLs (Fig. 1G). Furthermore, the binding capability of aFGF@NMLs for IL-1β and TNF-α that highly expressed during the sepsis-induced ALI was evaluated. The results showed aFGF@Lips was incapable of binding these cytokines, while aFGF@NMLs could significantly bind to pro-inflammatory cytokines (IL-1β and TNF-α). The levels of cytokines decreased with an increase in the aFGF@NMLs concentration, suggesting dose-dependent binding effects of the FGF@NMLs (Fig. 1 H,I).

3.2. Biocompatibility of aFGF@NMLs

Considering the biosafety of the application, the effects of the blank Lips and blank NMLs on cellular activity were initially evaluated. As illustrated in Fig. 2A,B, BEAS-2B cells incubated with various concentrations of blank Lips and blank NMLs all showed considerably high cell viability, indicating that this drug carrier had good cytocompatibility. The results of aFGF, aFGF@Lips, and aFGF@NMLs addition in the cytotoxicity assay showed cell viability improved with increasing additive concentrations, a result that could be attributed to the potent capability of aFGF to promote cell proliferation as shown in Fig. 2C–E. (Xie et al., 2011). During lung injury, pulmonary cells suffer extensive aberrant apoptosis, and regeneration of pulmonary epithelial cells is necessary to restore normal function of lung. Pathogenesis of many lung diseases is due to the lack of effective cell regeneration (Riemondy et al., 2019). Therefore, aFGF@NMLs with pro-cell proliferation property could promote the repair of injured lung tissues and accelerate disease recovery.

In addition, the hemocompatibilities of aFGF, aFGF@Lips, and aFGF@NMLs were also assessed before intravenous injection into the ALI model. As shown in Fig. 2F, no significant hemolysis was found in these treated groups. The calculated results showed the hemolysis rate of each group was quite low and fulfilled the safety requirements for animal experiments (Fig. 2G). To observe co-localization of aFGF and drug carrier, aFGF and NM were labeled with FITC and DiI, respectively. The image showed that the two different fluorescence overlapped, indicating the stable existence of the aFGF@NMLs in the medium (Fig. 2H).

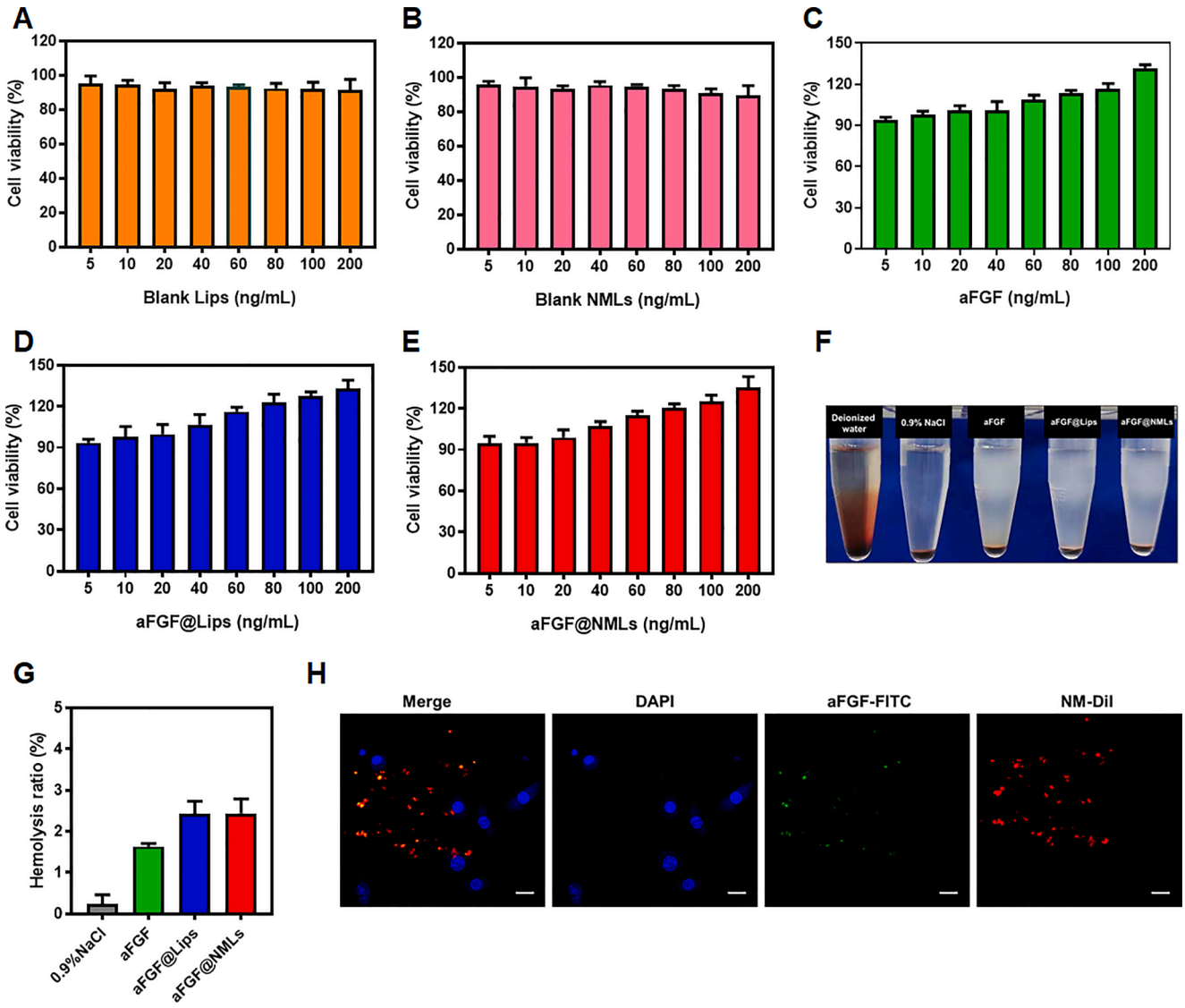

Fig. 2. Cytocompatibility and hemocompatibility of aFGF@NMLs. The BEAS-2B cell viability after incubating with various concentration of (A) blank Lips, (B) blank NMLs, (C) aFGF, (D) aFGF@Lips, and (E) aFGF@NMLs. (F) Hemocompatibility test and (G) hemolysis ratio. (H) Colocalization of fluorescein isothiocyanate (FITC)-labeled aFGF and DiI-labeled NM incubated with RAW 264.7 cells. Scale bar = 10 μm. Data are expressed as the mean ± SD (n = 3).

3.3. Cellular uptake of aFGF@NMLs

The BEAS-2B cells treated with or without LPS were incubated with FITC-labeled aFGF, aFGF@Lips, and aFGF@NMLs to detect cellular internalization. As shown in Fig. S2, cells not treated with LPS in each group all showed weak fluorescence, and no discernible difference between these groups was detected. However, in the LPS-treated cells group, the aFGF@NMLs group showed the highest fluorescent intensity among these groups (Fig. 3A). Furthermore, during the 4-h incubation period, cellular internalization of aFGF@NMLs was higher than that of free aFGF and aFGF@Lips at each time point and also exhibited a time-dependent uptake (Fig. 3B–D). In addition, the results of flow cytometry were consistent with the data of image (Fig. 3E), suggesting that aFGF@NMLs could be used as a vehicle for delivering aFGF into the inflamed pulmonary epithelial cells and enhancing cellular utilization of aFGF.

The bronchial epithelial cells exposed to LPS could produce large quantities of inflammatory cytokines, such as TNF-a, which drove cells to generate excessive ICAM-1. Overexpression of ICAM-1 on inflammation-injured cells specifically bound to LFA-1 on NM, thereby promoting aFGF@NMLs uptake by the inflamed BEAS-2B cells (Zhang et al., 2018). These findings revealed that the biomimetic aFGF@NMLs had a distinctive advantage over free aFGF and aFGF@Lips in terms of cellular uptake.

3.4. Cytoprotective effects of aFGF@NMLs

Excessive inflammatory reactions and oxidative stress can cause severe damage to lung cells during sepsis (Zhou et al., 2019b). To assess the cytoprotective of aFGF@NMLs on BEAS-2B cells suffering from inflammatory damage, LPS was used to stimulate cells that generated inflammatory response after which the anti-inflammatory effect of aFGF@NMLs were examined. First, an ROS fluorescent probe was used to observe the production of ROS in each group of cells. As shown in Fig. 4A&B, cells generated massive quantities of ROS after they were treated with LPS, which was accompanied by decrease in cell viability in LPS group (Fig. 4C). In the inflammatory environment, a significant accumulation of harmful MDA in the cells occurred while the activity of antioxidant enzymes decreased (Fig. 4D&E), indicating that the antioxidant system of the cells had been disrupted. In addition, secretion of HMGB-1, IL-1β and -6, and TNF-α were fairly high when compared to control group (Fig. 4F–I), and these pro-inflammatory cytokines showed

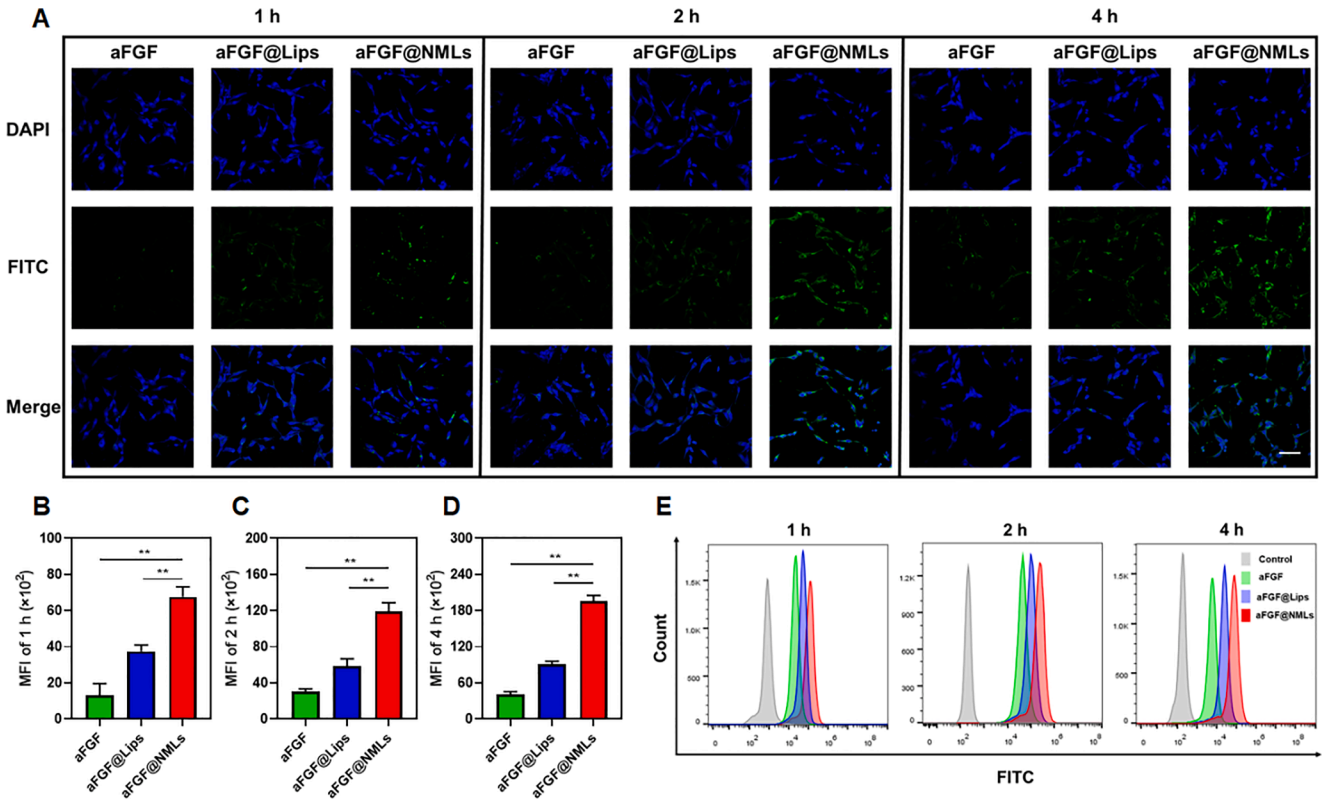

Fig. 3. Cellular uptake of aFGF@NMLs. (A) Representative images of the LPS-treated BEAS-2B cells incubated with aFGF, aFGF@Lips, or aFGF@NMLs for 1, 2, and 4 h. Scale bar = 50 μm. Quantification of mean fluorescent intensity (MFI) for (B) 1 h, (C) 2 h and (D) 4 h. (E) The flow cytometric analysis for cellular uptake of aFGF, aFGF@Lips, or aFGF@NMLs for 1, 2, and 4 h. Data are expressed as the mean ± SD (n = 3). *P ≤ 0.05, **P ≤ 0.01.

serious interference with the physiological metabolism of cells. Significantly, aFGF@NMLs effectively led to a reduction in intracellular ROS production and improvement in cell viability. Meanwhile, aFGF@NMLs led to a decrease in the MDA production in cells, enhancement of SOD activity, suppression of pro-inflammatory cytokine secretion, and protection of antioxidant and anti-inflammatory capacities of cells. Consistent with previous results, biomimetic aFGF@NMLs were more favorable for cellular uptake compared to aFGF and aFGF@Lips, which reinforced the pharmacological effects of aFGF. During sepsis, the lung has remarkable capacities to respond to injury by repairing and replacing damaged cells, which requires appropriate and timely inhibition of inflammation. Pulmonary epithelial cells play a key role in initiating and regulating lung tissue repair (Crosby and Waters, 2010). Thus, effective relief of inflammatory response in epithelial cells and maintenance of normal cell function is beneficial in the treatment of ALI.

3.5. Biodistribution of aFGF@NMLs

Neutrophils are the main inflammatory cells that dominate the progression of acute inflammation and early chronic inflammation, especially in ALI, in which excessive neutrophil infiltration in injured lung results in severe inflammatory destruction of the lung (Cui et al., 2019; Qin et al., 2019). In terms of this feature, aFGF@NMLs for pulmonary targeted therapy were constructed, and the targeting capability of FITC-labeled aFGF@NMLs was assessed using the IVIS small animal imaging system after injecting with the FITC-labeled aFGF and aFGF@Lips. As shown in Fig. 5A, strong fluorescent signals in the lung of ALI mice injected with aFGF@NMLs, could be observed, while faint fluorescent signals in the aFGF and aFGF@Lips groups at different time points were found. Quantitative analysis of fluorescent intensity showed that the fluorescent signals in the lung of all groups gradually decayed with time (Fig. 5B,C). Intra-pulmonary fluorescence in the aFGF group was almost negligible 8 h after injection. The aFGF@Lips group also showed weak fluorescence. In contrast, the lung of aFGF@NMLs group still retained considerable fluorescence (Fig. 5D). These results confirmed that aFGF@NMLs possessed powerful lung-targeting capability. Meanwhile, the levels of aFGF in blood after treatment with aFGF, aFGF@Lips, and aFGF@NMLs were also detected. As depicted in Fig. 5E, aFGF and aFGF@Lips had short circulation times and were rapidly depleted in blood, whereas aFGF@NMLs significantly enhanced the aFGF concentration in plasma and produced a longer circulation time. The results of *in vivo* distribution indicated that aFGF@NMLs was conducive for optimizing and promoting the distribution of aFGF in the damaged lung, increasing the concentration and retention time of aFGF at the lesion, amplifying the therapeutic effects of aFGF, and ultimately enhancing the repair and recovery of lung tissue.

The specific molecules on the surface of NM provided homologous targeting; this targeting mechanism is also widely used in targeted therapy for various types of tumors (Chen et al., 2021; Chen et al., 2016). Camouflage of cell membranes might effectively circumvent the immune system, extend the blood circulation of drug, and increase the drug accumulation in the focus area (Zhen et al., 2019). Utilizing the characteristics of the disease, this nanoplatform-based drug delivery strategy was found to provide significant benefits for treating ALI through enhancing therapeutic agent targeting and circulation.

3.6. Therapeutic effects of aFGF@NMLs in ALI

H&E staining was conducted to investigate the effects of aFGF@NMLs on lung histopathology and function in the ALI model. Compared to the control group, the ALI group showed pathological changes, including structural disorder of lung tissue and alveoli, and pulmonary interstitial edema and inflammatory cells excessively infiltrated the alveoli and interstitium. After treating cells with

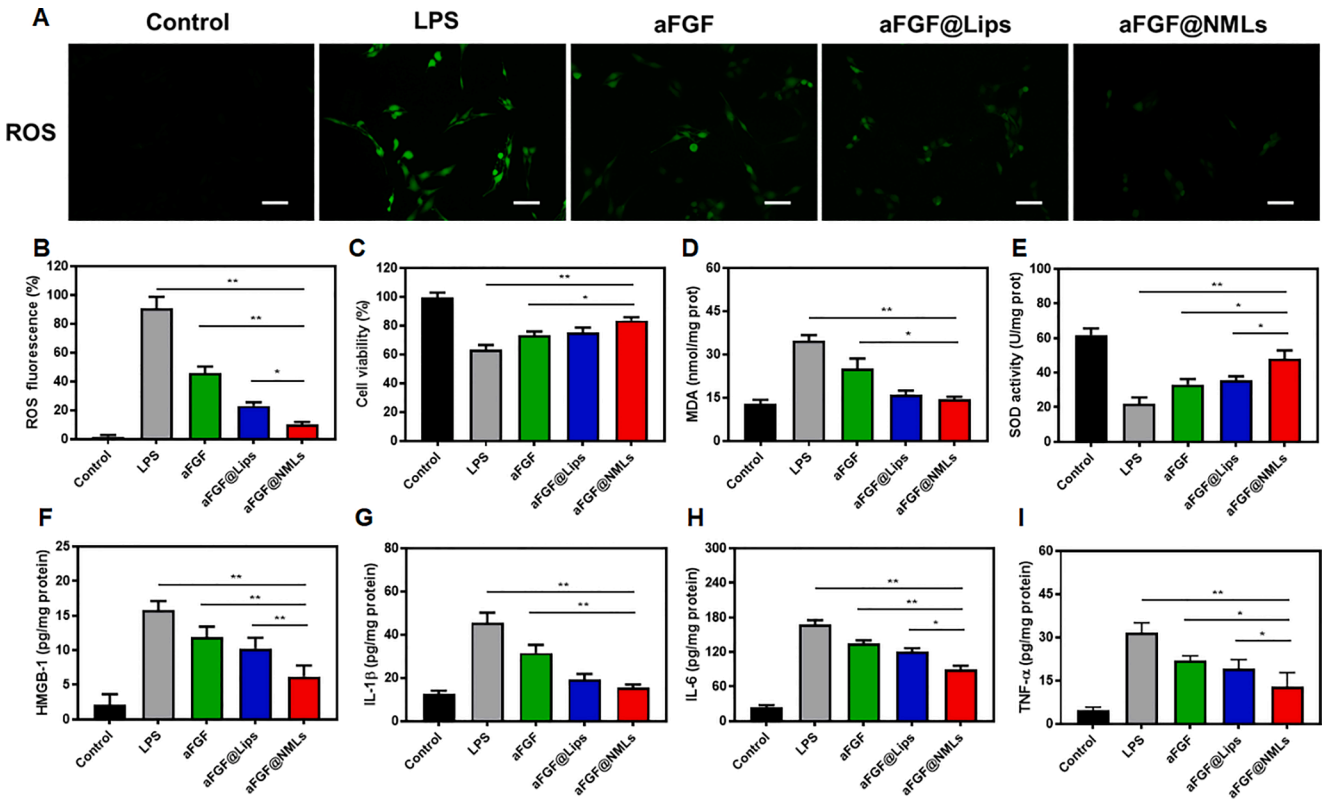

Fig. 4. Cytoprotective capability of aFGF@NMLs. (A) Representative images of intracellular reactive oxygen species (ROS) of lipopolysaccharide (LPS)-stimulated BEAS-2B cells after incubation with aFGF, aFGF@Lips, and aFGF@NMLs. Scale bar = 100 μm. (B) Quantitative analysis of ROS. (C) The cell viability of each group. The levels of (D) malondialdehyde (MDA) and (E) superoxide dismutase (SOD) in each group. The production of (F) high mobility box 1 (HMGB-1), (G) interleukin 1 beta (IL-1β), (H) IL-6, and (I) tumor necrosis factor alpha (TNF-α) of each group. Data are expressed as the mean ± SD (n = 3). *P ≤ 0.05, **P ≤ 0.01.

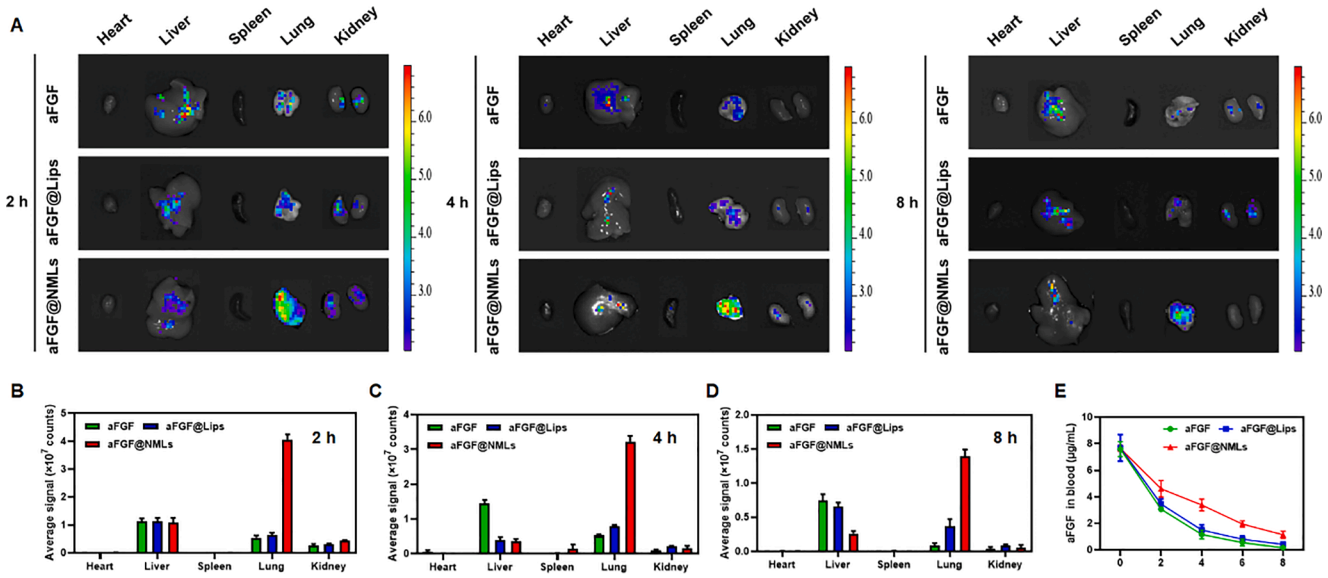

Fig. 5. *In vivo* distribution of aFGF@NMLs. (A) Biodistribution of aFGF, aFGF@Lips, and aFGF@NMLs in ALI mice at 2, 4, and 8 h after injection. The quantitative analysis of fluorescent signal in major organ at (B) 2 h, (C) 4 h and (D) 8 h. (E) The concentration of aFGF in blood after injection. Data are expressed as the mean ± SD (n = 3).

aFGF@NMLs, the lung tissue of ALI mice showed a decrease in the levels of alveolar congestion, inflammatory cell infiltration, and damage of tissue architecture (Fig. 6A). The results of pathological scoring reflected severe lung tissue damage in ALI group, whereas aFGF@NMLs evidently caused a decrease in lung injury scores and exerted lung-protective effects (Fig. 6C). Elevated inflammation and oxidative stress levels in damaged lungs exacerbated cell apoptosis (Chambers et al., 2018). As shown in Fig. 6B, intense fluorescence concentrated in the lung tissue of ALI group indicated that excessive cell apoptosis in the lung occurred. The quantitative fluorescent analysis revealed that a decrease in fluorescent intensity in lung of ALI model treated with aFGF and aFGF@Lips occurred, but obvious apoptosis still had occurred (Fig. 6D). By

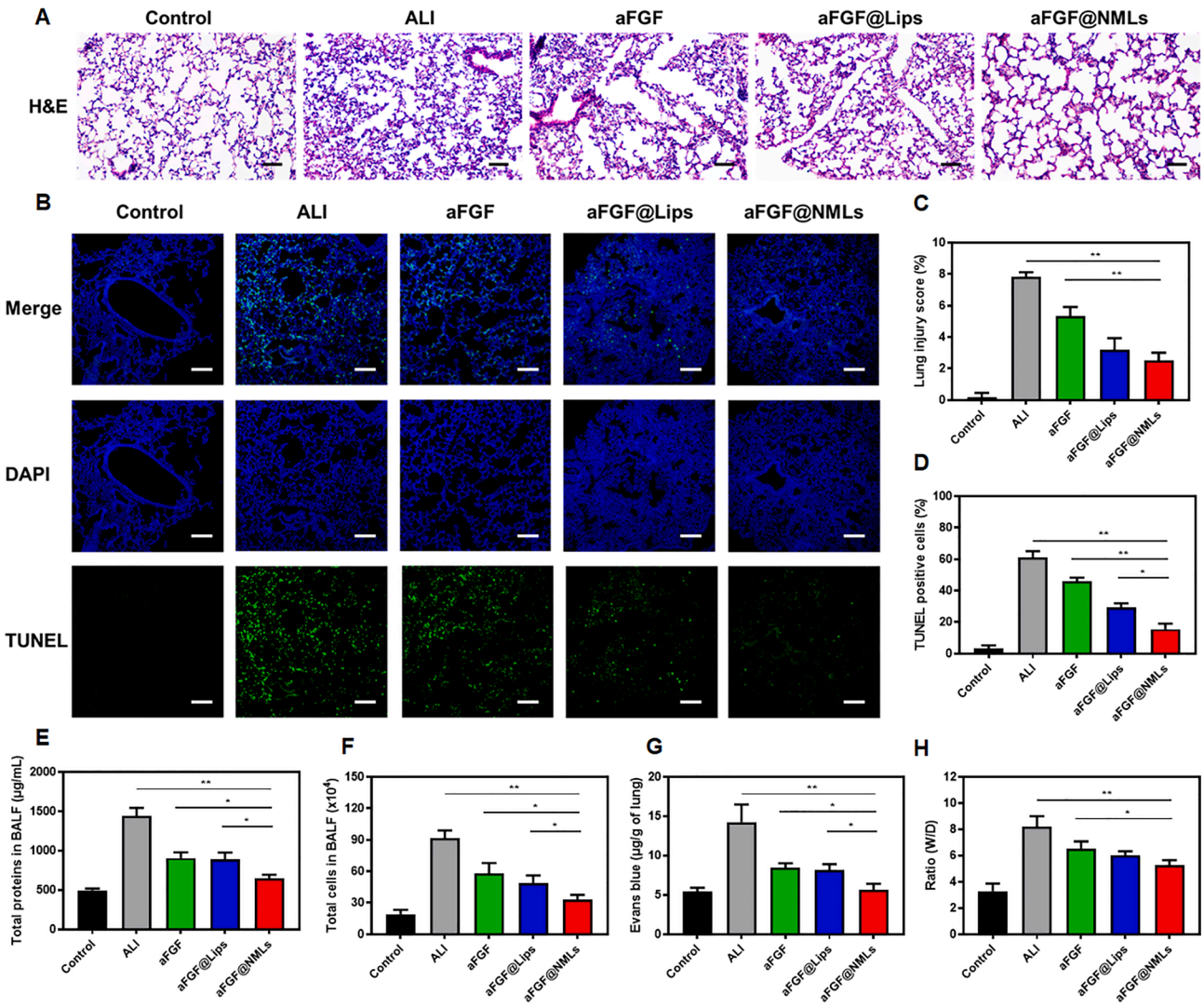

Fig. 6. Therapeutic efficacy of aFGF@NMLs. (A) Representative micrographs of H&E staining of lung. Scale bar = 100 μm. (B) The terminal deoxynucleotidyl transferase dUTP nick end labeling (TUNEL) immunofluorescent staining of lung. Scale bar = 100 μm. (C) The lung injury score of each group. (D) The quantitation of TUNEL positive cells. (E) The total protein and (F) cells in bronchoalveolar lavage fluid (BALF). (G) The content of Evans blue in lung. (H) The wet/dry weight (W/D) ratio of lung. Data are expressed as mean ± SD (n = 3). *P ≤ 0.05, **P ≤ 0.01. (For interpretation of the references to colour in this figure legend, the reader is referred to the web version of this article.)

comparison, aFGF@NMLs therapy caused a dramatic reduction in TUNEL fluorescence and ameliorated lung cell apoptosis.

Protein levels and cells in broncho alveolar lavage fluid (BALF) were also determined. An abnormal increase in vascular permeability in the injured lung during ALI that caused a large increase in fluid that was rich in protein and cells flowed into the lung (Keck et al., 2002). The content of protein and cell in BALF were unusually high in the ALI group, while the aFGF@NMLs group showed minimum levels of protein and cells in BALF among these treatment groups (Fig. 6E,F). In addition, Evans blue dye was used to determine the pulmonary vascular permeability of each group. The ALI group showed an elevated concentration of Evans blue in the lung, indicating enhanced pulmonary vascular permeability (Fig. 6G). The wet/dry (W/D) lung was also weighed to calculated W/D ratio that had increased in the ALI group, demonstrating severe pulmonary edema in the ALI mice (Fig. 6H). The aFGF@NMLs could cause a reduction in the Evans blue level and W/D ratio in ALI mice and protected the integrity of alveolar-capillary barrier, which suggested that alleviation of transvascular leakage in aFGF@NMLs group. These findings showed that aFGF@NMLs had a positive impact on the therapy of ALI.

3.7. Assessment of kidney and liver in ALI

In sepsis, kidney dysfunction is a nonnegligible factor, and renal hypotension and associated ischemia are the primary lesions in sepsis-related kidney injury (Poston and Koyner, 2019). Additionally, a deleterious inflammatory cascade was consistently observed in kidney during sepsis, indicating inflammation played vital roles in the pathogenesis of septic kidney injury. Circulating inflammatory cytokines can directly cause renal tissue damage (Bellomo et al., 2017). Meanwhile, endotoxin and other pathogen-associated molecular patterns can interact directly with relevant receptors on renal tubular cells, activate intracellular inflammatory pathways, and promote inflammatory responses in the kidney to cause acute tubular necrosis and tissue damaged (Zhong et al., 2020). Sepsis is also known to cause severe liver damage. Normal liver function is essential for treatment and recovery of patients with sepsis. Liver impairment caused by oxidative stress and dysregulation of inflammatory factors can lead to poor prognosis in a septic patient. Liver sinusoidal endothelial cells can respond to inflammatory signals that caused iNOS-dependent endothelial dysfunction, which leads to a reduction in vasodilatory responses to acetylcholine in liver. These pathological factors cause hypoxic liver injury (Yan et al., 2014). Thus,

the protective effects of aFGF@NMLs on kidney and liver were also investigated. As shown in Fig. 7A, the CD68 immunohistochemical analysis showed that substantial inflammation in kidney and liver had occurred during sepsis. Quantitative analysis of CD68-positive expression regions showed aFGF@NMLs also caused a reduction in inflammation levels in these tissues (Fig. 7B,C). In addition, aFGF@NMLs led to suppression of the inflammatory cytokine, TNF-α, production in kidney and liver (Fig. 7D,E). To evaluate liver and renal functions, levels of aspartate aminotransferase, alanine aminotransferase, creatinine, and blood urea nitrogen (AST, ALT, SCr, and BUN, respectively) in the blood from each group were also measured (Fig. 7F–I). The ALI group showed a sharp increase in the levels of these indicators when compared with the control group, and aFGF@NMLs treatment could cause a reduction in the levels of AST, ALT, SCr, and BUN, indicating that liver and kidney functions had recovered in ALI mice. These results confirmed that aFGF@NMLs also alleviated the inflammatory reactions in the kidney and liver during the sepsis, which then facilitated the treatment and recovery from sepsis.

3.8. The anti-inflammatory capacity of aFGF@NMLs in ALI

Sepsis-induced ALI is typically characterized by severe pulmonary inflammation that causes disruption of the alveolar-vascular endothelial barrier and the accumulation of neutrophils in the injured lung and released inflammatory mediators that cause alveolar congestion and metabolic disturbances (Xia et al., 2021). These pathological factors lead to impairment in gas exchange and alveolar surface function of the lung, and patients develop severe hypoxemia and elevated pulmonary artery wedge pressure. Current research generally recognizes that an uncontrolled inflammatory response caused by excessive activation and recruitment of inflammatory cells in the lung and many inflammatory factors activating and interacting with each other are the main pathological changes in ALI (Xia et al., 2021). Therefore, suppression of the excessive inflammatory response may be an essential strategy for treating ALI and regulating production of numerous pro-inflammatory factors in ALI is critical for early illness therapy and rapid reversal of poor prognosis (Song et al., 2021).

Immunohistochemical staining was performed, and the expression levels of these inflammation-associated cytokines were determined to evaluate the inflammatory levels in each group (Fig. 8A). In the ALI group, the macrophage marker, CD68, was extensively expressed in lung tissue indicating that the lung of mice in ALI group suffered severe inflammatory damage. After treatment with aFGF or aFGF@Lips, the inflammatory condition of the lung was relieved to some extent. Importantly, the aFGF@NMLs group showed negligible positive expression of CD68, which meant that aFGF@NMLs led to effective relief of inflammation in lung (Fig. 8B). In addition, the IL-6 and TNF-α were secreted extensively in the ALI group. aFGF and aFGF@Lips exhibited similar suppressive effects on inflammation, whereas lung-targeted aFGF@NMLs showed a superior anti-inflammatory activity (Fig. 8C,D). During the progressive phase of ALI, HMGB-1 released in large amounts and bound to the receptor of advanced glycation end products, led to activation of intracellular mitogen-activated protein kinases (MAPK) via intracellular tyrosine kinase or G protein-coupled receptor signaling pathways, which exacerbated inflammatory conditions (Qu et al., 2019). In the ALI group, HMGB-1 expression was clearly visible on the images, and the treatment groups all showed a decline in positive expression levels of HMGB-1, while aFGF@NMLs exerted

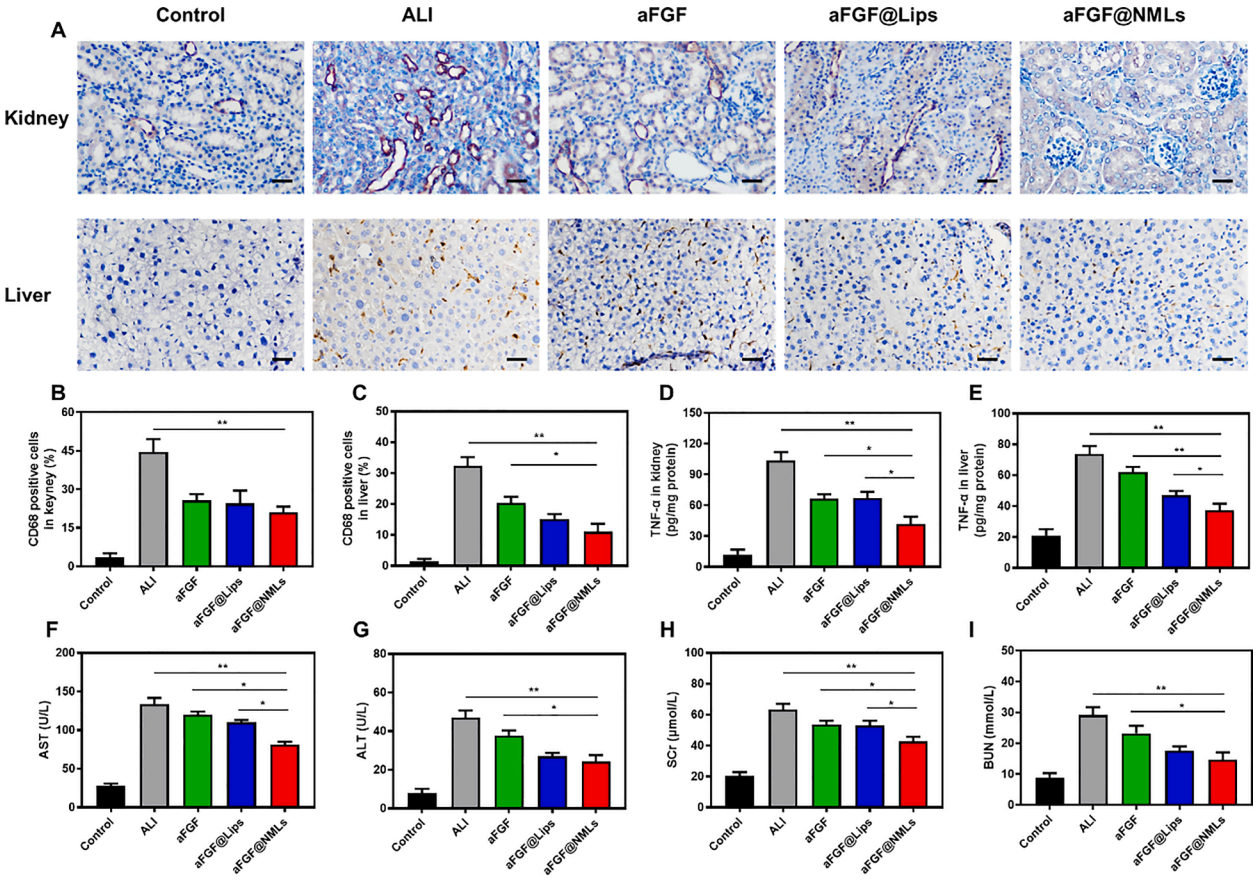

Fig. 7. Assessment of inflammation in kidneys and livers from ALI mice. (A) CD68 immunohistochemical staining in kidney and liver. Scale bar = 100 μm. The quantitation of positive cells of CD68 in (B) kidney and (C) liver. The levels of TNF-α in (D) kidney and (E) liver. The levels of (F) aspartate aminotransferase (AST), (G) alanine aminotransferase (ALT), (H) serum creatinine (SCr), and (I) blood urea nitrogen (BUN) of each group. Data are expressed as the mean ± SD (n = 3). *P ≤ 0.05, **P ≤ 0.01.

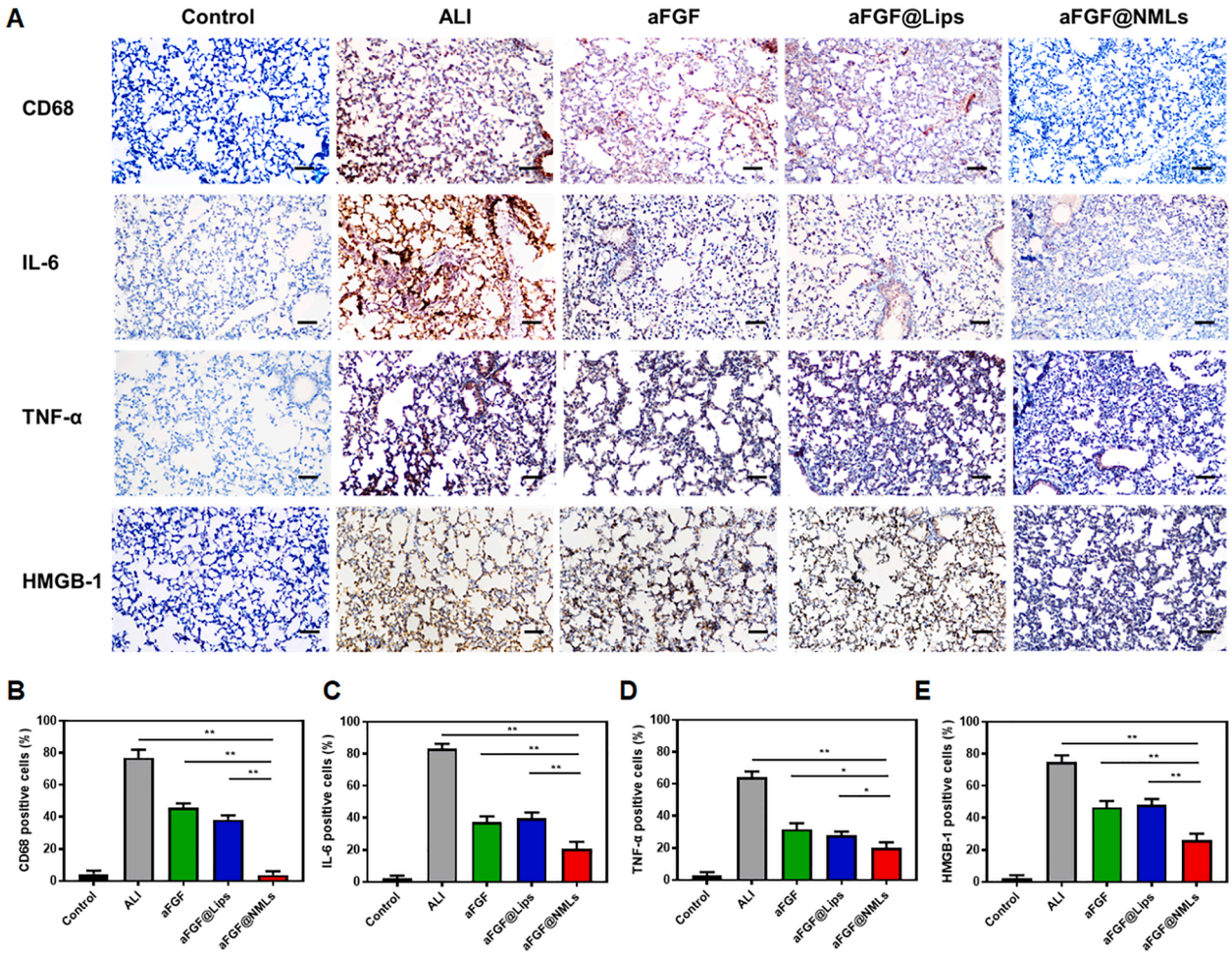

Fig. 8. The histological analysis of lung tissue. (A) CD68, IL-6, TNF-α, and HMGB-1 immunohistochemical staining of lung tissue. Scale bar = 100 μm. The quantitation of positive cells of (B) CD68, (C) IL-6 (D) TNF-α and (E) HMGB-1. Data are expressed as the mean ± SD (n = 3). *P ≤ 0.05, **P ≤ 0.01.

superior efficacy (Fig. 8E). The NM-coating preferentially transported the aFGF@NMLs to the inflamed lung to relieve the intense inflammation at the site of the lesion. These results demonstrated that biomimetic drug delivery aFGF@NMLs that specifically accumulate in injured lung have the capability of enhancing the pharmacological actions of aFGF for ALI.

4. Conclusion

In this work, a biomimetic strategy for delivery of aFGF is reported. The NM extracted from LPS-activated neutrophils and then coated with liposomes loaded with aFGF (aFGF@NMLs) were used for treating sepsis-induced ALI via alleviation of pulmonary inflammation. The results of ALI treatment showed that aFGF@NMLs selectively accumulated in the inflamed lung and led to a reduction in the severity of inflammation during sepsis-induced ALI. In addition, aFGF@NMLs also had mitigating effects on both sepsis-related liver and kidney injury and facilitated the recovery and prognosis of sepsis. This study confirmed that aFGF@NMLs promoted cellular uptake, optimized its distribution *in vivo*, and enhanced the pharmacological action of aFGF for treating ALI. Thus, this biomimetic drug carrier aFGF@NMLs offers a feasible modality for treatment of lung disorders, such as pulmonary inflammatory diseases and lung cancer.

CRediT authorship contribution statement

Zhiwei Huang: Methodology, Investigation, Writing – original draft. **Hengcai Wang:** Data curation. **Juan Long:** Formal analysis, Methodology. **Zhongqiu Lu:** Supervision, Funding acquisition. **Changju Chun:** Project administration, Validation. **Xinze Li:** Conceptualization, Methodology, Data curation, Writing – review & editing.

Declaration of Competing Interest

The authors declare that they have no known competing financial interests or personal relationships that could have appeared to influence the work reported in this paper.

Acknowledgements

This work was supported by National Natural Science Funds of China (Grant No. 81871583).

Appendix A. Supplementary material

Supplementary data to this article can be found online at https://doi.org/10.1016/j.ijpharm.2022.121971.

References

Bellomo, R., Kellum, J.A., Ronco, C., Wald, R., Martensson, J., Maiden, M., Bagshaw, S. M., Glassford, N.J., Lankadeva, Y., Vaara, S.T., Schneider, A., 2017. Acute kidney injury in sepsis. Intensive Care Med. 43 (6), 816–828.
Chambers, E., Rounds, S., Lu, Q., 2018. Pulmonary Endothelial Cell Apoptosis in Emphysema and Acute Lung Injury. Adv. Anat. Embryol. Cell Biol. 228, 63–86.

Chen, M., Bao, L., Zhao, M., Cao, J., Zheng, H., 2020a. Progress in Research on the Role of FGF in the Formation and Treatment of Corneal Neovascularization. Front. Pharmacol. 11, 111.
Chen, M., Cui, Y., Hao, W., Fan, Y., Zhang, J., Liu, Q., Jiang, M., Yang, Y., Wang, Y., Gao, C., 2021. Ligand-modified homologous targeted cancer cell membrane biomimetic nanostructured lipid carriers for glioma therapy. Drug Deliv. 28 (1), 2241–2255.
Chen, T., Zhu, G., Meng, X., Zhang, X., 2020b. Recent developments of small molecules with anti-inflammatory activities for the treatment of acute lung injury. Eur. J. Med. Chem. 207.
Chen, Z.e., Zhao, P., Luo, Z., Zheng, M., Tian, H., Gong, P., Gao, G., Pan, H., Liu, L., Ma, A., Cui, H., Ma, Y., Cai, L., 2016. Cancer Cell Membrane-Biomimetic Nanoparticles for Homologous-Targeting Dual-Modal Imaging and Photothermal Therapy. ACS Nano 10 (11), 10049–10057.
Crosby, L.M., Waters, C.M., 2010. Epithelial repair mechanisms in the lung. Am. J. Physiol. Lung Cell. Mol. Physiol. 298 (6), L715–L731.
Cui, A., Xiang, M., Xu, M., Lu, P., Wang, S., Zou, Y., Qiao, K., Jin, C., Li, Y., Lu, M., Chen, A.F., Chen, S., 2019. VCAM-1-mediated neutrophil infiltration exacerbates ambient fine particle-induced lung injury. Toxicol. Lett. 302, 60–74.
Fan, E., Brodie, D., Slutsky, A.S., 2018. Acute Respiratory Distress Syndrome: Advances in Diagnosis and Treatment. JAMA 319, 698–710.
Feng, L., Dou, C., Xia, Y., Li, B., Zhao, M., Yu, P., Zheng, Y., El-Toni, A.M., Atta, N.F., Galal, A., Cheng, Y., Cai, X., Wang, Y., Zhang, F., 2021. Neutrophil-like Cell-Membrane-Coated Nanozyme Therapy for Ischemic Brain Damage and Long-Term Neurological Functional Recovery. ACS Nano 15 (2), 2263–2280.
Gong, Y., Lan, H., Yu, Z., Wang, M., Wang, S., Chen, Y.u., Rao, H., Li, J., Sheng, Z., Shao, J., 2017. Blockage of glycolysis by targeting PFKFB3 alleviates sepsis-related acute lung injury via suppressing inflammation and apoptosis of alveolar epithelial cells. Biochem. Biophys. Res. Commun. 491 (2), 522–529.
Grommes, J., Soehnlein, O., 2011. Contribution of neutrophils to acute lung injury. Mol. Med. 17 (3-4), 293–307.
Huang, H.-W., Yang, C.-M., Yang, C.-H., 2021a. Fibroblast Growth Factor Type 1 Ameliorates High-Glucose-Induced Oxidative Stress and Neuroinflammation in Retinal Pigment Epithelial Cells and a Streptozotocin-Induced Diabetic Rat Model. Int. J. Mol. Sci. 22 (13), 7233.
Huang, Z.W., Shi, Y., Zhai, Y.Y., Du, C.C., Zhai, J., Yu, R.J., Kou, L., Xiao, J., Zhao, Y.Z., Yao, Q., 2021b. Hyaluronic acid coated bilirubin nanoparticles attenuate ischemia reperfusion-induced acute kidney injury. J. Control. Release 334, 275–289.
Jin, H., Zhao, Z., Lan, Q., Zhou, H., Mai, Z., Wang, Y., Ding, X., Zhang, W., Pi, J., Evans, C.E., Liu, X., 2020. Nasal Delivery of Hesperidin/Chitosan Nanoparticles Suppresses Cytokine Storm Syndrome in a Mouse Model of Acute Lung Injury. Front. Pharmacol. 11, 592238.
Jin, K., Luo, Z., Zhang, B.o., Pang, Z., 2018. Biomimetic nanoparticles for inflammation targeting. Acta Pharm Sin B. 8 (1), 23–33.
Kang, T., Zhu, Q., Wei, D., Feng, J., Yao, J., Jiang, T., Song, Q., Wei, X., Chen, H., Gao, X., Chen, J., 2017. Nanoparticles Coated with Neutrophil Membranes Can Effectively Treat Cancer Metastasis. ACS Nano 11 (2), 1397–1411.
Keck, T., Balcom, J.H., Castillo, C.F., Antoniu, B.A., Warshaw, A.L., 2002. Matrix metalloproteinase-9 promotes neutrophil migration and alveolar capillary leakage in pancreatitis-associated lung injury in the rat. Gastroent. 122 (1), 188–201.
Keszler, M., 2017. Mechanical ventilation strategies. Semin Fetal Neonatal Med. 22 (4), 267–274.
Liang, G., Song, L., Chen, Z., Qian, Y., Xie, J., Zhao, L., Lin, Q., Zhu, G., Tan, Y.i., Li, X., Mohammadi, M., Huang, Z., 2018. Fibroblast growth factor 1 ameliorates diabetic nephropathy by an anti-inflammatory mechanism. Kidney Int. 93 (1), 95–109.
Liu, Z., Liu, X., Yang, Q., Yu, L., Chang, Y., Qu, M., 2020. Neutrophil membrane-enveloped nanoparticles for the amelioration of renal ischemia-reperfusion injury in mice. Acta Biomater. 104, 158–166.
Mauri, T., Turrini, C., Eronia, N., Grasselli, G., Volta, C.A., Bellani, G., Pesenti, A., 2017. Physiologic Effects of High-Flow Nasal Cannula in Acute Hypoxemic Respiratory Failure. Am. J. Respir. Crit. Care Med. 195 (9), 1207–1215.
Park, I., Kim, M., Choe, K., Song, E., Seo, H., Hwang, Y., Ahn, J., Lee, S.H., Lee, J.H., Jo, Y.H., Kim, K., Koh, G.Y., Kim, P., 2019. Neutrophils disturb pulmonary microcirculation in sepsis-induced acute lung injury. Eur. Respir. J. 53.
Poston, J.T., Koyner, J.L., 2019. Sepsis associated acute kidney injury. BMJ 364, k4891.
Qin, X., Zhu, G., Huang, L., Zhang, W., Huang, Y., Xi, X., 2019. LL-37 and its analog FF/CAP18 attenuate neutrophil migration in sepsis-induced acute lung injury. J. Cell. Biochem. 120 (4), 4863–4871.
Qu, L., Chen, C., Chen, Y., Li, Y., Tang, F., Huang, H., He, W., Zhang, R., Shen, L., 2019. High-Mobility Group Box 1 (HMGB1) and Autophagy in Acute Lung Injury (ALI): A Review. Med. Sci. Monit. 25, 1828–1837.
Ren, Y., Li, L., Wang, M.M., Cao, L.P., Sun, Z.R., Yang, Z.Z., Zhang, W., Zhang, P., Nie, S. N., 2021. Pravastatin attenuates sepsis-induced acute lung injury through decreasing pulmonary microvascular permeability via inhibition of Cav-1/eNOS pathway. Int. Immunopharmacol. 100, 108077.
Riemondy, K.A., Jansing, N.L., Jiang, P., Redente, E.F., Gillen, A.E., Fu, R., Miller, A.J., Spence, J.R., Gerber, A.N., Hesselberth, J.R., Zemans, R.L., 2019. Single cell RNA sequencing identifies TGFbeta as a key regenerative cue following LPS-induced lung injury. JCI Insight 5.
Rittirsch, D., Huber-Lang, M.S., Flierl, M.A., Ward, P.A., 2009. Immunodesign of experimental sepsis by cecal ligation and puncture. Nat. Protoc. 4, 31–36.
Song, D., Zhao, M., Feng, L., Wang, P., Li, Y., Li, W., 2021. Salidroside attenuates acute lung injury via inhibition of inflammatory cytokine production. Biomed. Pharmacother. 142, 111949.
Sun, J., Huang, X., Niu, C., Wang, X., Li, W., Liu, M., Wang, Y., Huang, S., Chen, X., Li, X., Wang, Y., Jin, L., Xiao, J., Cong, W., 2021. aFGF alleviates diabetic endothelial dysfunction by decreasing oxidative stress via Wnt/beta-catenin-mediated upregulation of HXK2. Redox Biol. 39, 101811.
Sun, L.C., Zhang, H.B., Gu, C.D., Guo, S.D., Li, G., Lian, R., Yao, Y., Zhang, G.Q., 2018. Protective effect of acacetin on sepsis-induced acute lung injury via its anti-inflammatory and antioxidative activity. Arch Pharm Res. 41, 1199–1210.
Tu, H.J., Zhao, C.F., Chen, Z.W., Lin, W., Jiang, Y.C., 2020. Fibroblast Growth Factor (FGF) Signaling Protects Against Acute Pancreatitis-Induced Damage by Modulating Inflammatory Responses. Med. Sci. Monit. 26, e920684.
Wang, Q., He, Y., Zhao, Y., Xie, H., Lin, Q., He, Z., Wang, X., Li, J., Zhang, H., Wang, C., Gong, F., Li, X., Xu, H., Ye, Q., Xiao, J., 2017. A Thermosensitive Heparin-Poloxamer Hydrogel Bridges aFGF to Treat Spinal Cord Injury. ACS Appl. Mater. Interfaces 9, 6725–6745.
Wang, Y.M., Ji, R., Chen, W.W., Huang, S.W., Zheng, Y.J., Yang, Z.T., Qu, H.P., Chen, H., Mao, E.Q., Chen, Y., Chen, E.Z., 2019. Paclitaxel alleviated sepsis-induced acute lung injury by activating MUC1 and suppressing TLR-4/NF-kappaB pathway. Drug Des. Devel. Ther. 13, 3391–3404.
Wu, J.C., Huang, W.C., Chen, Y.C., Tu, T.H., Tsai, Y.A., Huang, S.F., Huang, H.C., Cheng, H., 2011. Acidic fibroblast growth factor for repair of human spinal cord injury: a clinical trial. J. Neurosurg Spine. 15, 216–227.
Wu, R., Dong, W., Zhou, M., Zhang, F., Marini, C.P., Ravikumar, T.S., Wang, P., 2007. Ghrelin attenuates sepsis-induced acute lung injury and mortality in rats. Am. J. Respir. Crit. Care Med. 176, 805–813.
Wu, X., Kong, Q., Zhan, L., Qiu, Z., Huang, Q., Song, X., 2019. TIPE2 ameliorates lipopolysaccharide-induced apoptosis and inflammation in acute lung injury. Inflamm. Res. 68, 981–992.
Xia, Y., Cao, Y., Sun, Y., Hong, X., Tang, Y., Yu, J., Hu, H., Ma, W., Qin, K., Bao, R., 2021. Calycosin Alleviates Sepsis-Induced Acute Lung Injury via the Inhibition of Mitochondrial ROS-Mediated Inflammasome Activation. Front. Pharmacol. 12, 690549.
Xie, L., Zhang, M., Dong, B., Guan, M., Lu, M., Huang, Z., Gao, H., Li, X., 2011. Improved refractory wound healing with administration of acidic fibroblast growth factor in diabetic rats. Diabetes Res. Clin. Pract. 93, 396–403.
Xie, W., Liu, P., Gao, F., Gu, Y., Xiao, Y., Wu, P., Chen, B., Liu, W., Liu, Q., 2022. Platelet-neutrophil hybrid membrane-coated gelatin nanoparticles for enhanced targeting ability and intelligent release in the treatment of non-alcoholic steatohepatitis. Nanomedicine 102538.
Xiong, S., Hong, Z., Huang, L.S., Tsukasaki, Y., Nepal, S., Di, A., Zhong, M., Wu, W., Ye, Z., Gao, X., Rao, G.N., Mehta, D., Rehman, J., Malik, A.B., 2020. IL-1beta suppression of VE-cadherin transcription underlies sepsis-induced inflammatory lung injury. J. Clin. Invest. 130, 3684–3698.
Xu, H.-L., Chen, P.-P., Wang, L.-F., Xue, W., Fu, T.-L., 2018. Hair regenerative effect of silk fibroin hydrogel with incorporation of FGF-2-liposome and its potential mechanism in mice with testosterone-induced alopecia areata. J. Drug Del. Sci. Technol. 48, 128–136.
Yan, J., Li, S., Li, S., 2014. The role of the liver in sepsis. Int. Rev. Immunol. 33, 498–510.
Zemans, R.L., Colgan, S.P., Downey, G.P., 2009. Transepithelial migration of neutrophils: mechanisms and implications for acute lung injury. Am. J. Respir. Cell Mol. Biol. 40, 519–535.
Zhang, Q., Dehaini, D., Zhang, Y., Zhou, J., Chen, X., Zhang, L., Fang, R.H., Gao, W., Zhang, L., 2018. Neutrophil membrane-coated nanoparticles inhibit synovial inflammation and alleviate joint damage in inflammatory arthritis. Nat. Nanotechnol. 13, 1182–1190.
Zhao, Y.Z., Zhang, M., Wong, H.L., Tian, X.Q., Zheng, L., Yu, X.C., Tian, F.R., Mao, K.L., Fan, Z.L., Chen, P.P., Li, X.K., Lu, C.T., 2016. Prevent diabetic cardiomyopathy in diabetic rats by combined therapy of aFGF-loaded nanoparticles and ultrasound-targeted microbubble destruction technique. J. Control. Release 223, 11–21.
Zhao, Y.Z., ZhuGe, D.L., Tong, M.Q., Lin, M.T., Zheng, Y.W., Jiang, X., Yang, W.G., Yao, Q., Xiang, Q., Li, X.K., Xu, H.L., 2019. Ulcerative colitis-specific delivery of keratinocyte growth factor by neutrophils-simulated liposomes facilitates the morphologic and functional recovery of the damaged colon through alleviating the inflammation. J. Control. Release 299, 90–106.
Zhen, X., Cheng, P., Pu, K., 2019. Recent Advances in Cell Membrane-Camouflaged Nanoparticles for Cancer Phototherapy. Small 15, e1804105.
Zheng, Q., Wang, Y.C., Liu, Q.X., Dong, X.J., Xie, Z.X., Liu, X.H., Gao, W., Bai, X.J., Li, Z. F., 2020. FK866 attenuates sepsis-induced acute lung injury through c-jun-N-terminal kinase (JNK)-dependent autophagy. Life Sci. 250, 117551.
Zhong, Y., Wu, S., Yang, Y., Li, G.Q., Meng, L., Zheng, Q.Y., Li, Y., Xu, G.L., Zhang, K.Q., Peng, K.F., 2020. LIGHT aggravates sepsis-associated acute kidney injury via TLR4-MyD88-NF-kappaB pathway. J. Cell Mol. Med. 24, 11936–11948.
Zhou, X., Cao, X., Tu, H., Zhang, Z.R., Deng, L., 2019a. Inflammation-Targeted Delivery of Celastrol via Neutrophil Membrane-Coated Nanoparticles in the Management of Acute Pancreatitis. Mol. Pharm. 16, 1397–1405.
Zhou, Y., Li, P., Goodwin, A.J., Cook, J.A., Halushka, P.V., Chang, E., Zingarelli, B., Fan, H., 2019b. Exosomes from endothelial progenitor cells improve outcomes of the lipopolysaccharide-induced acute lung injury. Crit. Care 23, 44.